The electronic structure of the high-symmetry perovskite iridate Ba_2IrO_4

2014 New J. Phys. 16 013008

(http://iopscience.iop.org/1367-2630/16/1/013008)

New Journal of Physics
The open access journal at the forefront of physics
Deutsche Physikalische Gesellschaft DPG | IOP Institute of Physics

The electronic structure of the high-symmetry perovskite iridate Ba_2IrO_4

S Moser[1,2,6], L Moreschini[2], A Ebrahimi[1], B Dalla Piazza[1], M Isobe[3], H Okabe[3], J Akimitsu[4], V V Mazurenko[5], K S Kim[2], A Bostwick[2], E Rotenberg[2], J Chang[1], H M Rønnow[1] and M Grioni[1]

[1] Institute of Condensed Matter Physics (ICMP), Ecole Polytechnique Fédérale de Lausanne (EPFL), CH-1015 Lausanne, Switzerland
[2] Advanced Light Source (ALS), Lawrence Berkeley National Laboratory, Berkeley, CA 94720, USA
[3] National Institute for Materials Science (NIMS), 1-1 Namiki, Tsukuba, Ibaraki 305-0044, Japan
[4] Department of Physics and Mathematics, Aoyama Gakuin University, 5-10-1 Fuchinobe, Chuo-ku, Sagamihara, Kanagawa 252-5258, Japan
[5] Theoretical Physics and Applied Mathematics Department, Ural Federal University, Mira Street19, 620002 Ekaterinburg, Russia
E-mail: simon.moser@epfl.ch

Received 4 October 2013, revised 27 November 2013
Accepted for publication 2 December 2013
Published 9 January 2014
New Journal of Physics **16** (2014) 013008
doi:10.1088/1367-2630/16/1/013008

Abstract

We report angle-resolved photoemission (ARPES) measurements, density functional and model tight-binding calculations on Ba_2IrO_4 (Ba-214), an antiferromagnetic ($T_N = 230$ K) insulator. Ba-214 does not exhibit the rotational distortion of the IrO_6 octahedra that is present in its sister compound Sr_2IrO_4 (Sr-214), and is therefore an attractive reference material to study the electronic structure of layered iridates. We find that the band structures of Ba-214 and Sr-214 are qualitatively similar, hinting at the predominant role of the spin–orbit interaction in these materials. Temperature-dependent ARPES data show that the energy gap persists well above T_N, and favor a Mott over a Slater scenario for this compound.

[6] Author to whom any correspondence should be addressed.

1. Introduction

The iridates are a new family of strongly correlated materials, with fascinating physical properties [1–12]. Unlike 3d transition metal oxides (TMOs), dominated by the Coulomb interaction, or 4d TMOs, where Hund's rule coupling plays a major role [13], the electronic structure of the 5d iridates reflects the coexistence of similar Coulomb, crystal-field (CEF) and spin–orbit (SO) coupling energy scales. As a result, Mott physics and local magnetic moments can emerge in the iridates for values of the Coulomb interaction that are one order of magnitude smaller than in the 3d series.

The layered perovskite Sr_2IrO_4 (Sr-214) has attracted considerable attention because of intriguing similarities with the cuprate parent compound La_2CuO_4 (LCO). Structurally, it exhibits weakly coupled IrO_2 square-lattice planes built from corner-sharing IrO_4 plaquettes, analogous to the characteristic CuO_4 building blocks of the cuprates [4, 5, 14–16]. The electronic structure is shaped by strong SO coupling, which splits the Ir 5d t_{2g}^5 manifold, so that the highest occupied state is a narrow, half-filled $j_{\rm eff} = 1/2$ band. The Ir spins order into an antiferromagnetic (AFM) state below $T_N = 230$–240 K. According to the leading scenario, Sr-214 is an insulator because a Mott gap $\Delta \sim 0.06$ eV opens within this band, but the actual origin of the gap is still being debated. An alternative Slater picture, coupling the onset of magnetic order with the opening of a gap [17, 18], has been advocated by susceptibility, time-resolved optical conductivity and scanning tunneling spectroscopy data [19, 20, 23, 24].

One may speculate that Sr-214 could be turned into a superconductor by doping, similarly to LCO. However, superconductivity is hindered by weak in-plane ferromagnetism, attributed to the Dzyaloshinsky–Moriya interaction, which arises from a rotational distortion of the IrO_6 octahedra (figure 1(a)). Recently, the sister compound Ba_2IrO_4 (Ba-214), with similar physical properties (table 1), was synthesized using high pressure methods [20] (figure 2(b)). Due to the larger Ba radius, Ba-214 does not exhibit the rotational distortion, and is therefore a more promising parent compound for possible iridate superconductors. Ba-214 also offers the possibility of studying the electronic structure of an undistorted IrO_2 square lattice.

We present here an investigation of Ba-214 by angle-resolved photoelectron spectroscopy (ARPES). We analyze the experimental data with the help of first-principles density functional theory (DFT) and model tight-binding (TB) band structure calculations. We find that the band structure of Ba-214 is quite similar to that of Sr-214, and is therefore rather insensitive to the presence of the rotational distortion. We also observe a backfolding of the band structure corresponding to a larger $c(2 \times 2)$ in-plane unit cell, that coincides with the AFM unit cell. ARPES data collected over a broad temperature range do not give evidence for a temperature-dependent gap, and therefore are more consistent with a Mott than with a Slater scenario.

2. Methods

Samples of Ba-214 were grown as in [20] in the form of dense, black polycrystalline pellets. The pellets were broken into clusters of $\sim$1 mm^3 size, and then dipped in 1% hydrofluoric acid for 1 min. After rinsing in deionized water, single crystals of $\sim$400 μm lateral size could be extracted. Crystals naturally exposing the (001) surface were selected under an optical microscope and mounted on ceramic pins.

The ARPES measurements were performed at the electronic structure factory end station of beam line 7 of the Advanced Light Source, Lawrence Berkeley National Laboratory. The

Table 1. Comparison of structural, magnetic and electronic properties in Ba_2IrO_4 and Sr_2IrO_4. d_b and d_{ap} are the in-plane and apical Ir–O distances.

	d_b (Å)	d_{ap} (Å)	θ_{tilt}	T_N (K)	μ (μ_B)	E_a (meV)	Ref.
Ba_2IrO_4	2.01	2.15	0°	230	0.34	70	[20]
Sr_2IrO_4	1.98	2.06	11°	230–240	0.33	60	[2, 14, 16]

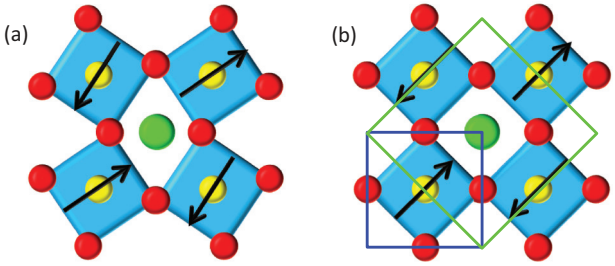

Figure 1. (a) Sr_2IrO_4 structure, projected on the *ab* plane (red = O; green = Sr; and yellow = Ir). Apical oxygen atoms are not shown. Each IrO_6 octahedron is rotated by 11° around the perpendicular *c*-axis with respect to the ideal K_2NiF_4 structure, yielding a larger $c(2 \times 2)$ unit cell. The distortion is absent in Ba_2IrO_4 (b) (green = Ba). The arrows illustrate the Ir spin arrangement in the AFM phase. Blue and green squares are the primitive and magnetic unit cell [21, 22].

combined energy resolution of the monochromator and of the Scienta R4000 hemispherical analyzer was ~30 meV. Samples were cleaved at $T \sim 100$ K at a pressure $< 10^{-10}$ mbar. The Fermi level reference was measured on polycrystalline copper in good electrical equilibrium with the sample. Sample charging hindered measurements below ~80 K. All data presented here were collected at $T \geqslant 120$ K, where the effect was smaller and under control. The data were subsequently corrected for the residual energy shift, which was estimated from a comparison with data measured in a low-filling mode of the storage ring, with a photon intensity reduced by almost two orders of magnitude.

3. Angle-resolved photoemission results

3.1. Band structure

Figure 2(a) presents an ARPES constant energy (CE) map of Ba-214, measured at $E = -0.1$ eV, near the top of the valence band. The map is extracted from a dataset measured at photon energy $h\nu = 155$ eV, and $T = 130$ K. The blue square is the surface Brillouin zone (BZ) corresponding to the crystallographic unit cell of figure 1(b) [20]. The map shows intense round features (α features in the following) at the M points, the corners of the BZ. A second set of features (β features), with fourfold symmetry, is observed at the X points. Both α and β features are repeated in all BZs of the map. A closer inspection reveals also a weaker, round contour (α^*) at all Γ points. It will be clear in the following that α^* is a signature of band folding into the smaller $c(2 \times 2)$ BZ (green square).

Figures 2(b)–(d) show the experimental E versus $k_\parallel$ dispersion along high-symmetry lines marked (b), (c) and (d) in figure 2(a). Along $M\Gamma M$, figure 2(b) shows a prominent band with a maximum at the M point, where it gives rise to the α contour. As discussed below, this

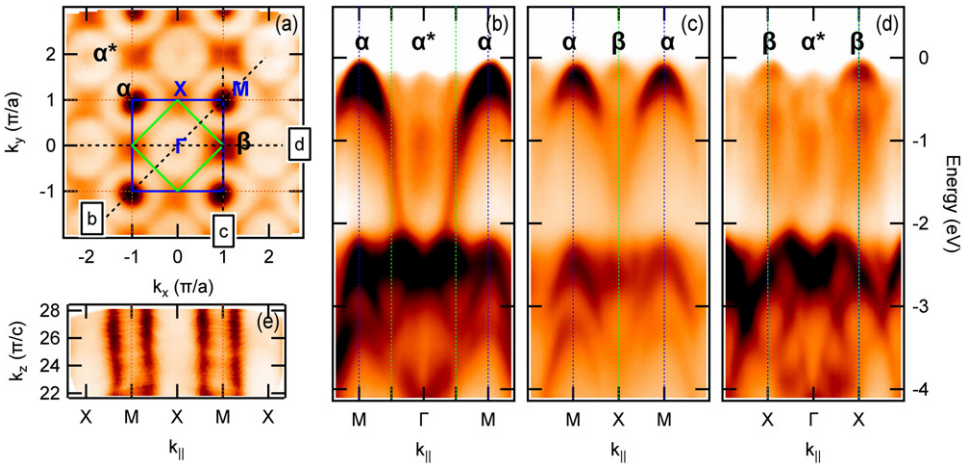

Figure 2. (a) ARPES k_x versus k_y CE map of Ba-214, measured at $E = -0.1$ eV with $h\nu = 155$ eV at $T = 130$ K. It shows intense features centered at the M and X points of the surface BZ (blue square), and a weaker replica of the former at Γ. The green square is the $c(2 \times 2)$ BZ. (b)–(d) E versus $k_{\|}$ cuts along the high symmetry directions indicated as (b), (c) and (d) in panel (a). Blue and green vertical lines indicate the boundaries of the (1×1) and of the $c(2 \times 2)$ BZs. (e) ARPES k_x versus k_z CE map at $E = -0.4$ eV and $k_y = \pi/a$, extracted from a photon energy scan between 95 and 162 eV, assuming an inner potential $V_0 = 10$ eV. It shows negligible dispersion along the c-axis. $\Gamma X = \pi/a = 0.78$ Å^{-1}; $\Gamma Z = \pi/c = 0.24$ Å^{-1}. In all panels, the darkest features correspond to the largest intensity.

band corresponds primarily to Ir states of $j_{\text{eff}} = 3/2$ character. It merges around -2 eV with a manifold of O 2p-derived states. The same band is seen to disperse downwards along the MXM direction in figure 2(c). A second band, with a maximum at the X point, generates the β contour. In the Mott scenario, it is assigned to the Ir-derived lower-Hubbard band of $j_{\text{eff}} = 1/2$ character. The maxima of this band are more visible along the $X\Gamma X$ direction in figure 2(d), which also shows a dispersive feature with a maximum at Γ, associated with the α^* contour. Figure 2(e) shows a k_x versus k_z CE map for $E = -0.4$ eV and $k_y = \pi/a$. It is extracted from ARPES measurements with photon energies in the range $h\nu = 95$–162 eV, assuming an inner potential $V_0 = 10$ eV. Apart from slight intensity variations with photon energy, the data are essentially independent of k_z. Namely, the absence of wiggling contours indicates that the k_z dispersion at the top of the valence band (VB), and the interplane coupling for these states, are quite small.

Representative spectra for the Γ, M and X points of the BZ are shown in figure 3. They exhibit rather broad peaks, with maxima at -0.37 eV (at Γ), -0.26 eV (at M), and -0.21 eV (at X), which places the VB maximum at the X point. The peak energy at the VB maximum should yield a lower limit for the energy gap, the actual value depending on the separation between the Fermi level and the conduction band minimum, which cannot be accessed by ARPES. However, the peak binding energy at X (0.21 eV) is already larger than the gap value $\Delta_g \simeq 2E_a \sim 140$ meV, estimated from the activation energy $E_a = 70$ meV of the electrical resistivity [20]. This discrepancy, and the broad line shapes, suggest unresolved overlapping features in the spectra of figure 3. This hypothesis is supported by the first-principles calculations of section 4.1. It also explains the different peak energies measured at

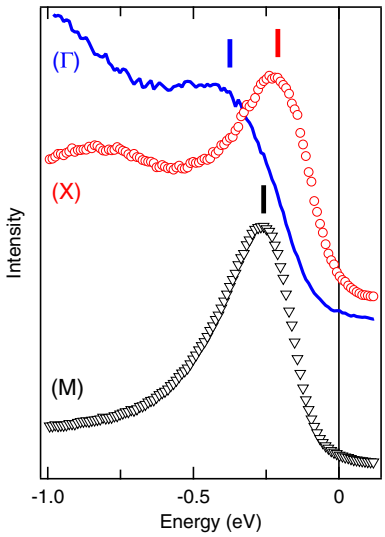

Figure 3. ARPES spectra of Ba-214, measured at three high symmetry points of the BZ. The corresponding peak positions are indicated by vertical lines.

the top of the band at the M point, and at its backfolded replica at Γ, since the underlying components can be differently modulated by matrix elements.

We now compare the electronic structure of Ba-214 and Sr-214. Figure 4(a) reproduces ARPES data on Sr-214 from [4]. The spectra are measured along the $\Gamma M' X'$ contour in the $c(2 \times 2)$ BZ, indicated by a yellow triangle in the top panel. Our results for Ba-214, extracted from the dataset of figure 2, are shown for the same triangular contour in figure 4(b). Data measured along the same triangular contour in the adjacent $c(2 \times 2)$ BZ are also shown in figure 4(c). Two conclusions can be drawn from the figure. Firstly, there is a good overall correspondence between the band structure of the two compounds. Secondly, while the relative intensities of the Ba-214 $j_{\mathrm{eff}} = 3/2$ and $1/2$ bands in figures 4(b) and (c) are different, their dispersions are identical. The triangular contours in figures 4(b) and (c) are equivalent for the $c(2 \times 2)$ BZ, but clearly not for the structural BZ (blue square). This shows that—similarly to the case of Sr-214 [4]—the band structure of Ba-214 is folded into the smaller BZ. The smaller intensity of the α^* manifold in figure 4(b), compared with that of the α manifold in figure 4(c), is consistent with band folding from a superlattice potential that is substantially weaker than the primary lattice potential [25]. The different intensities in the two contours can be exploited to disentangle the two bands. We find that in Ba-214 the width of the $j_{\mathrm{eff}} = 1/2$ band (∼0.8 eV) is somewhat larger than in Sr-214 (∼0.5 eV) [4], and is considerably smaller than the width of the $j_{\mathrm{eff}} = 3/2$ band (∼2.5 eV). The maxima of the $j_{\mathrm{eff}} = 1/2$ band at X (−0.21 eV) and of the $j_{\mathrm{eff}} = 3/2$ band at M (−0.26 eV) in Ba-214 are shallower than those (−0.25 eV and, respectively −0.45 eV) of the corresponding bands in Sr-214. Their energy separation is also smaller (0.05 versus 0.2 eV) in Ba-214.

3.2. Temperature evolution

We now address the issue, raised in the introduction, of the persistence of the energy gap above $T_{\mathrm{N}} \sim 240$ K. Previous theoretical and experimental studies [18, 23, 24] have claimed significant Slater-type contributions to the stability of the gap, which should then collapse in

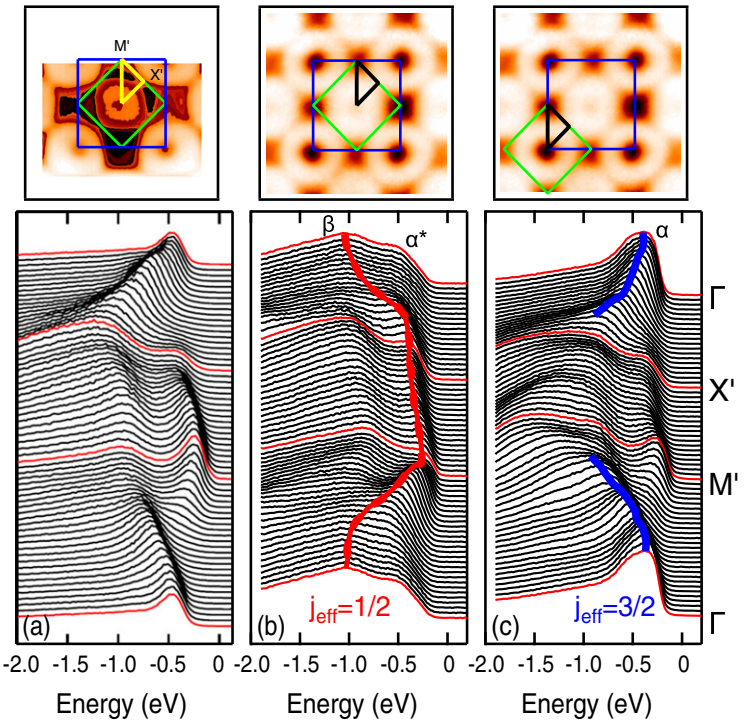

Figure 4. (a) ARPES spectra of Sr-214, measured along the $\Gamma M' X'$ contour (yellow triangle) in the $c(2 \times 2)$ BZ (green square), from [4]. Data for Ba-214, extracted from figure 2, are shown along the same contour in (b), and for an equivalent contour in an adjacent $c(2 \times 2)$ BZ in (c). Spectra corresponding to the high-symmetry points are in red. Matrix elements enhance the signal from $j_{\text{eff}} = 1/2$ states in (b), and from $j_{\text{eff}} = 3/2$ states in (c). Thick red (b) and blue (c) curves outline their dispersion.

the paramagnetic phase. We collected data over a broad temperature range, from well below (120 K) to well above (300 K) T_{N}. Figure 5 displays temperature-dependent ARPES spectra measured at the Γ and M points of the BZ. The leading edge of the spectra exhibits a trivial thermal broadening, but no indications that the gap closes at T_{N}. The energy gap appears to be robust even in the absence of long-range magnetic order. Therefore, the ARPES data do not support a Slater picture, at least in its simplest form.

4. Electronic structure calculations

4.1. First-principles calculations

We performed a local density approximation (LDA) calculation including the on-site Coulomb and SO interactions (LDA + U + SO) [29]. For this purpose, the linear muffin-tin orbital approach in the atomic sphere approximation (Stuttgart LMTO47 code) [30] was used, with crystal structure data taken from [20]. We include Ba(6s,6p,5d), Ir(6s,6p,5d) and O(2s,2p) states in the orbital basis set. Both the ferromagnetic (FM) and AFM configurations were simulated for different sets of on-site Ir 5d Coulomb repulsion U and intra-atomic exchange interaction J_{H}. The FM configuration is calculated with one Ir atom per unit cell. In order to reproduce the AFM order observed in Ba_2IrO_4, we have used a supercell containing four Ir atoms. The

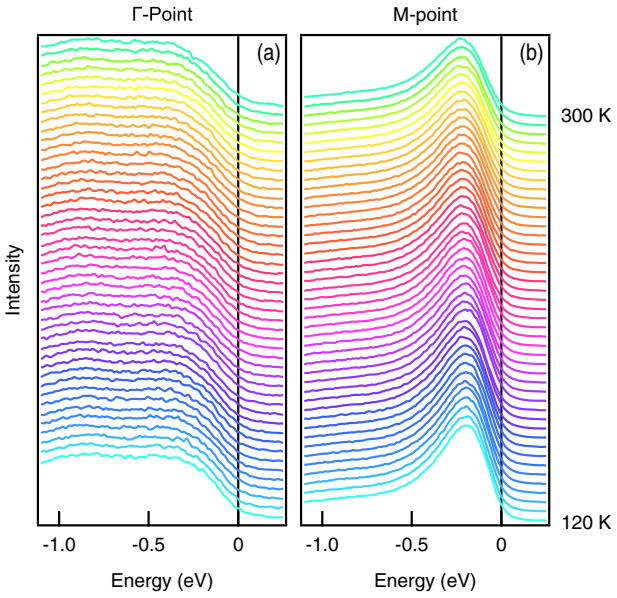

Figure 5. Temperature-dependent ARPES spectra of Ba-214 from $T = 120$ to 300 K, measured at (a) the Γ, and (b) the M points of the BZ.

primitive lattice vectors in units of $a = 4.03$ Å are $(0, 2, 0)$, $(2, 0, 0)$ and $(0.5, 0.5, -1.65)$. In the AFM configuration, $U = 3$ eV and $J_{\mathrm{H}} = 0.4$ eV produced the correct energy gap value of 140 meV. The same values were recently used in [12].

The calculated band structure is illustrated in figure 6(a), superimposed on the ARPES data. Overall, DFT yields many more states than ARPES can individually resolve, which probably explains the absence of sharp quasiparticle features in the spectra. The partial densities of states of figure 6(b) show that Ir 5d and 2p in-plane oxygen states are strongly hybridized at the top of the valence band, while the bottom of the conduction band is mainly formed by Ir 5d electrons. The 2p states of the apical oxygen atoms are confined between -1 and -2 eV, due to a limited overlap with the Ir 5d orbitals. These states have a non-negligible dispersion along the c-axis. The band observed in ARPES around -3 eV corresponds to in-plane 2p oxygen states.

We now briefly discuss the implications of the DFT results for the magnetic properties of Ba-214. Firstly, we emphasize that the occupied states close to the gap at the Γ and M points strongly depend on the specific magnetic configuration. For instance, in the FM state the top of the valence band is found at $E \simeq -0.7$ eV (not shown). Moreover, a FM insulating ground state with the correct energy gap could only be obtained for unreasonably large values of U and J_{H}. Therefore, the inter-site exchange interaction plays a decisive role in determining the band structure close to the Fermi level.

Within the LDA + U + SO approximation [29] the electronic Hamiltonian matrix and the corresponding occupation matrix of the system can be defined in the $\{LS\}$ basis (the eigenfunctions of both spin and orbital moment operators) or $\{jm_j\}$ basis (the total moment operator eigenfunctions). They correspond to LS (Russell–Saunders) or jj coupling schemes. The basis choice becomes important when one calculates the expectation value of the magnetic moment to compare it with experimental data. In this case, either the LS coupling scheme or the jj coupling scheme should be chosen, depending on the strength of the SO coupling. However, when the SO coupling and the intra-atomic exchange interaction are comparable, neither the

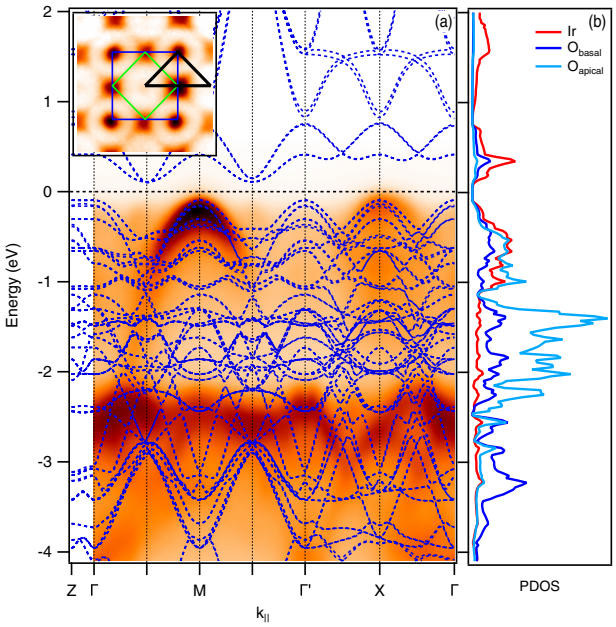

Figure 6. (a) The LDA + U + SO band structure is superimposed on an ARPES intensity map, where an integral Shirley background has been subtracted. The bands were calculated for the AFM configuration with $U = 3$ eV and $J_H = 0.4$ eV. Apical oxygen states between -1 and -2 eV are not resolved in the experiment. (b) Partial densities of states. Red, dark and light blue lines correspond to Ir 5d, in-plane oxygen 2p and apical oxygen 2p states, respectively.

LS nor the jj scheme are valid, and an intermediate coupling theory should be developed [29]. Practically, it means that the occupation matrix is neither diagonal in the $\{LS\}$ nor in $\{jm_j\}$ orbital basis. Such a situation is realized in Ba-214, where the SO strength $\lambda \sim 0.48$ eV and $J_H \sim 0.4$ eV.

Within an $\{LS\}$ eigenstates basis we obtain for the spin and orbital magnetic moments $M_S = 0.12\,\mu_B$ and $M_L = 0.33\,\mu_B$, respectively. The resulting total magnetic moment is therefore $M_{LS} = (2M_S + M_L) = 0.57\,\mu_B$, in reasonable agreement with the value $M = 0.36\,\mu_B$ from magnetic susceptibility measurements [20]. The total magnetic moment calculated within a $\{jm_j\}$ basis is equal to $M_J = 0.43\,\mu_B$, in better agreement with the experimental value. However, one should note that in both basis sets there are large non-diagonal elements of the occupation matrix that do not contribute to the expectation value of the magnetic moment. Therefore, an intermediate coupling scheme should be used to correctly describe the magnetism of Ba-214. We leave such a consideration for a future investigation.

The performed first-principles calculations have demonstrated a complicated band structure depending on the metal–ligand hybridization, on-site Coulomb interaction, SO coupling, intra- and inter-atomic exchange interactions. The agreement between all-electron LDA + U + SO and experimental ARPES spectra is not enough to determine the exact microscopic mechanisms that are responsible for forming the electronic structure of Ba_2IrO_4. To solve this problem below we propose a tight-binding model with a minimal set of orbitals.

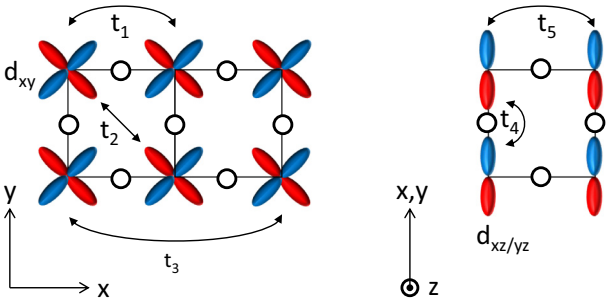

Figure 7. Effective hopping terms for the Ir t_{2g} states used in the TB model: (a) d_{xy} orbitals and (b) $d_{xz/yz}$ orbitals. Empty circles represent oxygen ions.

4.2. Tight binding approach

In order to gain more direct insight in the interplay of orbital ordering, SOC and correlation effects, we also performed a model TB calculation, along the lines of [27, 28]. We included the whole Ir 5d t_{2g} and e_g manifolds, and a set of effective hopping terms describing the hybridization between the Ir 5d and O 2p electrons, as illustrated in figure 7. The tight binding Hamiltonian is

$$H = H_0 + H_{SO}. \tag{1}$$

H_0 includes the kinetic term $T = \Sigma_{k,\nu}\, \varepsilon_\nu(k) c^\dagger_{k\nu} c_{k\nu}$, where $c^\dagger_k$ and c_k are the fermion creation and annihilation operators and ν spans the Ir 5d manifold, and an octahedral CEF parameterized by $10Dq = E(e_g) - E(t_{2g})$. Since we are primarily interested in the occupied states for a comparison with ARPES, we focus on the t_{2g} levels. The relevant hopping terms are schematically illustrated in figure 7. The form of the ε_ν's is dictated by the symmetry of the system [27]:

$$\begin{aligned}
\varepsilon_{xy} &= -2t_1(\cos k_x + \cos k_y) - 2t_2 \cos k_x \cos k_y - 2t_3(\cos 2k_x + \cos 2k_y),\\
\varepsilon_{xz} &= -2t_4 \cos k_x - 2t_5 \cos k_y,\\
\varepsilon_{yz} &= -2t_5 \cos k_x - 2t_4 \cos k_y.
\end{aligned} \tag{2}$$

The SO coupling term for the 5d orbitals is: $H_{SO} = \lambda_{5d} \vec{L} \cdot \vec{S}$. We introduce electron correlations in the model in a phenomenological way, by imposing AFM order. This is achieved by an additional Zeeman term with an in-plane staggered magnetic field

$$H_{AFM} = B \sum_{i,\nu} e^{i\vec{Q}\cdot\vec{r}_i} \left(c^\dagger_{i\nu\uparrow} c_{i\nu\downarrow} + c^\dagger_{i\nu\downarrow} c_{i\nu\uparrow} \right), \tag{3}$$

where $\vec{Q} = (\pi, \pi)$ is the AFM ordering vector, and the sum is over the Ir sites i and the three t_{2g} orbitals. The effect of H_{AF} is to fold all bands into the smaller $c(2 \times 2)$ BZ, and to open gaps at the AFM zone boundaries.

The band structures produced by the various terms of the hamiltonian are plotted in figure 8(a)–(c), along the same $\Gamma X' M' \Gamma$ contour of figures 4(a) and (b). The parameters of the model are summarized in table 2. Figures 8(a′)–(c′) schematically illustrate the local electronic structure at the Ir site. Figure 8(a) shows the band dispersion in the presence of the octahedral CEF. The empty e_g and the partially filled t_{2g} manifolds are well separated by $10Dq$, and the

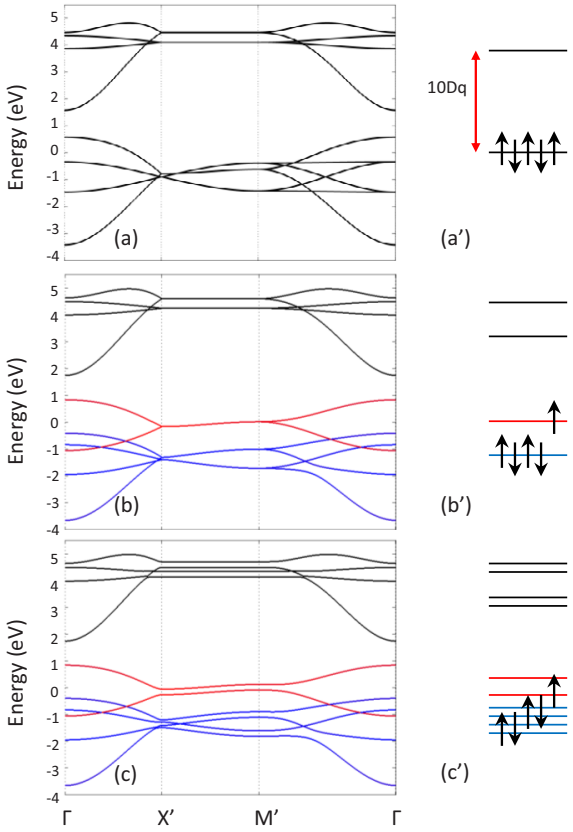

Figure 8. The calculated TB band structure is shown in (a) in the presence of an octahedral CEF. In (b) the addition of SO coupling rearranges the bands into $j_{\rm eff} = 3/2$ (blue) and $j_{\rm eff} = 1/2$ (red) states. A staggered magnetic field splits all states in (c), namely within the half-filled $j_{\rm eff} = 1/2$ band, simulating the opening of the Mott gap. Panels (a′–c′) are corresponding schematic pictures of the local electronic structure at the Ir sites.

Table 2. The set of parameters (in eV) of the TB model used for the calculated band structure of figures 8 and 9.

λ_{5d}	t_1	t_2	t_3	t_4	t_5	B
0.7	0.5	0.1	0.03	0.27	0.01	0.1

system is metallic. Adding the SO interaction, in figures 8(b) and (b′), mixes the CEF states. The t_{2g} states are split into a four-fold degenerate, fully occupied $j_{\rm eff} = 3/2$ (blue), and a doubly degenerate, half-filled, $j_{\rm eff} = 1/2$ manifold (red), but the system remains metallic. Figures 8(c) and (c′) illustrate the further band splitting induced by $H_{\rm AFM}$, namely of the $j_{\rm eff} = 1/2$ band into $m_j = -1/2$ and $1/2$ subbands, which effectively simulates the opening of a correlation gap between an occupied lower Hubbard band and an empty upper Hubbard band.

The calculated TB band structure is compared with the ARPES data in figure 9 for the set of parameters of table 2. Although the TB parameters, namely the external magnetic field, should not be taken too literally, they do provide a useful description of the electronic structure.

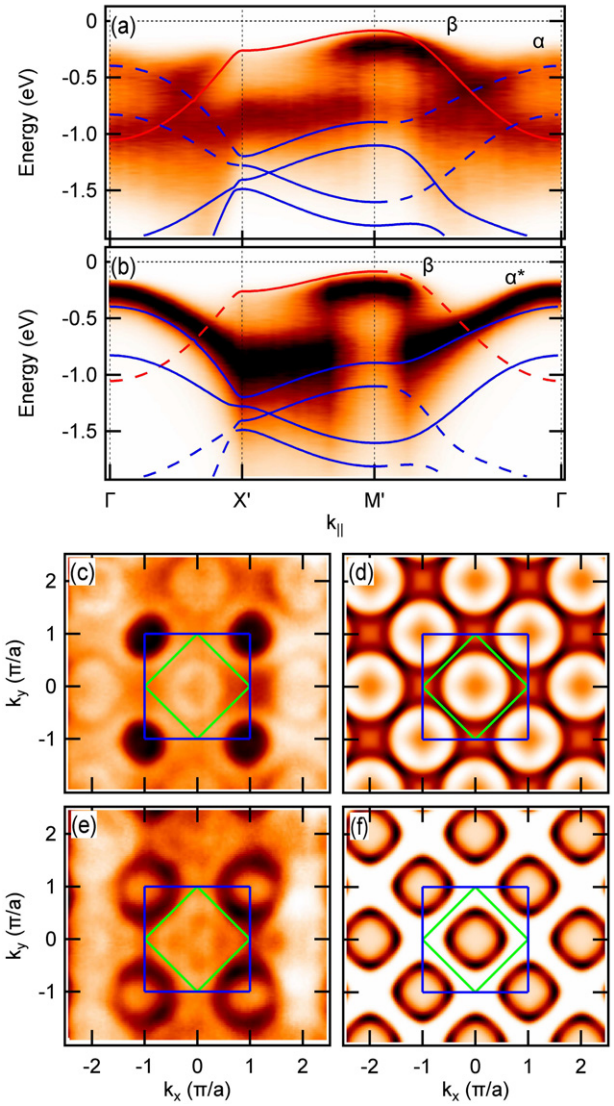

Figure 9. The calculated TB band structure is superimposed on the experimental ARPES data, along two equivalent contours in the first (a) and in an adjacent (b) $c(2 \times 2)$ BZ, as in figure 4(b), (c). Folded bands are indicated by dashed lines. The color code is the same as in figure 8. Panels (c), (d) show the experimental (c) and calculated (d) CE maps for $E = -0.35$ eV. The corresponding CE maps for $E = -0.7$ eV are shown in (e), (f).

Figures 9(a) and (b) show data along equivalent contours in the first and in the adjacent $c(2 \times 2)$ BZs, as in figures 4(b) and (c). Folded bands are indicated by dashed lines. The good agreement with the data substantiates the description of the bands given in section 3, namely the assignment of the top of the valence band to states of $j_{\mathrm{eff}} = 1/2$ character. The good agreement of the TB model with the experiment is confirmed by a comparison of the experimental and calculated CE maps shown in figures 9(c) and (d) and figures 9(e) and (f), for $E = -0.35$ eV (c, d) and $E = -0.7$ eV (e, f). The experimental α (α^*) and β features are well reproduced. Of course, the TB model does not yield any information on the spectral weight, and therefore all $c(2 \times 2)$ BZs are equivalent.

5. Summary

We have measured the electronic structure of the perovskite iridate Ba_2IrO_4 (Ba-214) by ARPES on high-quality single crystal samples grown under high pressure. A comparison of spectra measured at non-equivalent locations of reciprocal space allows us to unambiguously identify the $j_{\rm eff} = 3/2$ and $1/2$ subbands into which the Ir 5d t_{2g} manifold is split by the SO interaction. The experimental data are well reproduced by an LDA + U + SO calculation for an AFM configuration. A satisfactory agreement is also achieved by a simple empirical tight-binding model. The overall band dispersion is similar to that of the sister compound Sr-214. The electronic structure is therefore rather insensitive to the rotational distortion of the IrO_6 octahedra, which is present in Sr-214 but not in Ba-214. This observation contrasts with the behavior of 3d TM perovskites, such as the rare earth nickelates $RNiO_3$, where the tilting of the octahedra, which affects the orbital overlap, strongly influences the band dispersion, as well as transport and magnetic properties [31]. This lends support to a proposed scenario for the iridates, where the effective hopping parameters are less sensitive to the distortion due to the strong mixing of d_{xy}, d_{xz} and d_{yz} orbital characters induced by the SO interaction [26].

We have also found that the bands measured by ARPES are folded, with reduced intensity, into a smaller $c(2 \times 2)$ BZ, producing a characteristic checkerboard intensity distribution. Band folding has also been observed in Sr-214 [4], and attributed to the effect of the structural distortion. Very sensitive x-ray diffraction measurements with synchrotron radiation rule out a structural distortion in the bulk of Ba-214 [32]. Our results are consistent with the periodicity of the AFM structure, and could indicate scattering of the quasiparticles by the corresponding superlattice potential. However, we cannot exclude that a structural distortion develops at the surface, which has indeed been suggested by low-energy electron diffraction measurements on thin film samples [33]. Accurate surface x-ray diffraction experiments are necessary to determine the surface structure of Ba-214, and resolve this issue.

Finally, we have studied the evolution with temperature of the energy gap, and found no notable variations, namely around the magnetic ordering temperature $T_{\rm N} = 230$ K. The gap remains open well into the paramagnetic phase. The ARPES data are therefore more consistent with a Mott than with a Slater scenario, even if our calculations indicate a clear influence of magnetic order on the size of the gap.

Acknowledgments

We gratefully acknowledge insightful discussions with V I Anisimov, A O Shorikov, B J Kim, D F McMorrow, S Boseggia and C Tournier-Colletta. Special thanks are due to K M Shen for sharing with us his unpublished data. The work at Lausanne is supported by the Swiss NSF LM was supported by the Swiss NSF Grant N PA00P21-36420. The work of VVM is supported by the grant program of President of Russian Federation MK-5565.2013.2 and the contract of the Ministry of Education and Science of Russia N 14.A18.21.0076. The Advanced Light Source is supported by the Director, Office of Science, Office of Basic Energy Sciences, of the US Department of Energy under contract no. DE-AC02-05CH11231.

References

[1] Cao G, Bolivar J, McCall S, Crow J E and Guertin R P 1998 *Phys. Rev.* B **57** 11039
[2] Kini N S, Strydom A M, Jeevan H S, Geibel C and Ramakrishnan S 2006 *J. Phys.: Condens. Matter* **18** 8205

[3] Moon S J *et al* 2008 *Phys. Rev. Lett* **101** 226402
[4] Kim B J *et al* 2008 *Phys. Rev. Lett* **101** 076402
[5] Kim B J, Ohsumi H, Komesu T, Sakai S, Morita T, Takagi H and Arima T 2009 *Science* **323** 1329
[6] Ge M, Qi T F, Korneta O B, De Long L E, Schlottmann P, Crummet W P and Cao G 2011 *Phys. Rev.* B **84** 100402
[7] Qi T F, Korneta O B, Chikara S, Ge M, Parkin S, De Long L E, Schlottmann P and Cao G 2011 *J. Appl. Phys.* **109** 07D906
[8] Wang F and Senthil T 2011 *Phys. Rev. Lett.* **106** 136402
[9] Fujiyama S, Ohsumi H, Komesu T, Matsuno J, Kim B J, Takata M, Arima T and Takagi H 2012 *Phys. Rev. Lett.* **108** 247212
[10] Haskel D, Fabbris G, Zhernenkov M, Kong P P, Jin C Q, Cao G and van Veenendaal M 2012 *Phys. Rev. Lett.* **109** 027204
[11] Cetin M F, Lemmens P, Gnezdilov V, Wulferding D, Menzel D, Takayama T, Ohashi K and Takagi H 2012 *Phys. Rev.* B **85** 195148
[12] Comin R *et al* 2012 *Phys. Rev. Lett.* **109** 226406
[13] Georges A, de' Medici L and Mravlje J 2013 *Annu. Rev. Condens. Matter Phys.* **4** 137
[14] Crawford M K, Subramanian M A, Harlow R L, Fernandez-Baca J A, Wang Z R and Johnston D C 1994 *Phys. Rev.* B **49** 9198
[15] Kim J, Casa D, Upton M H, Gog T, Kim Y J, Mitchell J F, van Veenendaal M, Daghofer M, van den Brink J and Khaliullin G 2012 *Phys. Rev. Lett.* **108** 177003
[16] Shimura T, Inaguma Y, Nakamura T, Itoh M and Morii Y 1995 *Phys. Rev.* B **52** 9143
[17] Gebhard F 1997 *The Mott Metal–Insulator Transition: Models and Methods* (Heidelberg: Springer)
[18] Arita R, Kunes J, Kozhevnikov A V, Eguiluz A G and Imada M 2012 *Phys. Rev. Lett.* **108** 086403
[19] Moon S J, Jin H, Choi W S, Lee J S, Seo S S A, Yu J, Cao G, Noh T W and Lee Y S 2009 *Phys. Rev.* B **80** 195110
[20] Okabe H, Isobe M, Takayama-Muromachi E, Koda A, Takeshita S, Hiraishi M, Miyazaki M, Kadono R, Miyake A and Akimitsu J 2011 *Phys. Rev.* B **83** 155118
[21] Boseggia S, Walker H C, Vale J, Springell R, Feng Z, Perry R S, Moretti Sala M, Rønnow H M, Collins S P and McMorrow D F 2013 *J. Phys.: Condens. Matter* **25** 422202
[22] Boseggia S, Springell R, Walker H C, Rønnow H M, Rüegg Ch, Okabe H, Isobe M, Perry R S, Collins S P and McMorrow D F 2013 *Phys. Rev. Lett.* **110** 117207
[23] Hsieh D, Mahmood F, Torchinsky D H, Cao G and Gedik N 2012 *Phys. Rev.* B **86** 035128
[24] Li Q *et al* 2013 arXiv:1303.7265
[25] Voit J, Perfetti L, Zwick F, Berger H, Margaritondo G, Grüner G, Höchst H and Grioni M 2000 *Science* **290** 501
[26] Katukuri V M, Stoll H, van den Brink J and Hozoi L 2012 *Phys. Rev.* B **85** 220402
[27] Watanabe H, Shirakawa T and Yunoki S 2010 *Phys. Rev. Lett.* **105** 216410
[28] Martins C, Aichorn M, Vaugier L and Biermann S 2011 *Phys. Rev. Lett.* **107** 266404
[29] Shorikov A O, Lukoyanov A V, Korotin M A and Anisimov A I 2005 *Phys. Rev.* B **72** 024458
[30] Andersen O K 1975 *Phys. Rev.* B **12** 3060
[31] Torrance J B, Lacorre P, Nazzal A I, Ansaldo E J and Niedermayer C 1992 *Phys. Rev.* B **45** 8209
[32] McMorrow D F private communication
[33] Shen K M private communication